LANGMUIR

Subscriber access provided by University of South Dakota

Biological and Environmental Phenomena at the Interface

Efficient propulsion and hovering of bubble-driven hollow micromotors underneath an air-liquid interface

Leilei Wang, Li Chen, Jing Zhang, Jinming Duan, Lei Wang, Zhanhua Silber-Li, Xu Zheng, and Haihang Cui

Langmuir, **Just Accepted Manuscript** • DOI: 10.1021/acs.langmuir.8b02249 • Publication Date (Web): 09 Aug 2018

Downloaded from http://pubs.acs.org on August 15, 2018

Just Accepted

“Just Accepted” manuscripts have been peer-reviewed and accepted for publication. They are posted online prior to technical editing, formatting for publication and author proofing. The American Chemical Society provides “Just Accepted” as a service to the research community to expedite the dissemination of scientific material as soon as possible after acceptance. “Just Accepted” manuscripts appear in full in PDF format accompanied by an HTML abstract. “Just Accepted” manuscripts have been fully peer reviewed, but should not be considered the official version of record. They are citable by the Digital Object Identifier (DOI®). “Just Accepted” is an optional service offered to authors. Therefore, the “Just Accepted” Web site may not include all articles that will be published in the journal. After a manuscript is technically edited and formatted, it will be removed from the “Just Accepted” Web site and published as an ASAP article. Note that technical editing may introduce minor changes to the manuscript text and/or graphics which could affect content, and all legal disclaimers and ethical guidelines that apply to the journal pertain. ACS cannot be held responsible for errors or consequences arising from the use of information contained in these “Just Accepted” manuscripts.

ACS Publications

is published by the American Chemical Society. 1155 Sixteenth Street N.W., Washington, DC 20036

Published by American Chemical Society. Copyright © American Chemical Society. However, no copyright claim is made to original U.S. Government works, or works produced by employees of any Commonwealth realm Crown government in the course of their duties.

Efficient propulsion and hovering of bubble-driven hollow micromotors underneath an air-liquid interface

Lei-lei Wang, † *Li Chen,* † *Jing Zhang,* † *Jin-ming Duan,* † *Lei Wang,* † *Zhan-hua Silber-Li,* ‡ *Xu Zheng,* *‡ *and Hai-hang Cui** †

†School of Environment and Municipal Engineering, Xi'an University of Architecture and Technology, Xi'an, 710055, China.

‡State Key Laboratory of Nonlinear Mechanics, Institute of Mechanics, Chinese Academy of Science, Beijing, 100190, China.

ABSTRACT

Bubble-driven micromotors have attracted substantial interest due to their remarkable self-motile and cargo-delivering abilities in biomedical or environmental applications. Here, we developed a hollow micromotor that experiences fast self-propulsion underneath an air-liquid interface by periodic bubble growth and collapse. The collapsing of a single microbubble induces an ~1 $m\cdot s^{-1}$ impulsive jetting flow that instantaneously pushes the micromotor forward. Unlike previously reported micromotors propelled by the recoiling of bubbles, cavitation-induced jetting further utilizes the energy stored in the bubble to propel the micromotor, and thus enhances the energy conversion efficiency by three orders of magnitude. Four different modes of propulsion are, for the first time, identified by quantifying the dependence of propulsion strength on microbubble size. Meanwhile, the vertical component of the jetting flow counteracts the buoyancy of the micromotor-bubble dimer and facilitates counterintuitive hovering underneath the air-liquid interface. This work not only enriches the understanding of the propulsion mechanism of bubble-driven micromotors but also gives insight into the physical aspects of cavitation bubble dynamics near the air-liquid interface on the microscale.

INTRODUCTION

The autonomous motion of artificial micromotors has attracted great attention over the past decades owing to their potential applications in biomedical[1-6] and environmental areas.[7, 8] Among existing micromotors, one main category is catalytic micromotors that convert chemical energy into mechanical motion based on the local chemical reaction at the surface, such as the bimetallic nanorods[9, 10] and insulator-catalyst Janus microspheres.[11, 12] One main challenge of designing high-efficiency micromotors is to overcome the restrictions inherent to propulsion in a viscous flow with a low Reynolds number ($\mathrm{Re} = uL/\nu$, where u, L and ν are the typical velocity, typical flow dimension and kinetic viscosity of the fluid, respectively).

For a small platinum-silica (Pt-SiO_2) Janus micromotor (JM) with a size of ~1 μm, phoretic propulsion emerges when the JM is immersed in a H_2O_2 solution to create a nonuniform concentration field as a result of the decomposition of H_2O_2 on the Pt side.[11 13, 14] However, the speed and propulsion efficiency are sometimes too low for engineering applications.[15] As first reported for tubular micromotors,[16, 17] bubble propulsion achieves the highest speed among all kinds of micromotors.[15, 18] In a system similar to the aforementioned Pt-SiO_2 JM but with a larger size (~10 μm), microbubbles can nucleate and grow near the Pt surface. The periodic emergence of the bubbles and the interaction between the bubbles and the JM enable symmetry-breaking in microscale viscous flows with a low Re number and induce fast motion of the JM.[19, 20]

In contrast to previous studies that only focused on the direct momentum exchange between a JM and microbubbles during bubble growth and recoiling stages,[21-25] the hydrodynamic effect during the bubble collapse stage should be given more attention when considering the dramatic variation of the flow field in a short time. So far, a detailed propulsion mechanism for the different stages of the entire lifetime of a bubble is still lacking. For example, a good understanding of the hydrodynamic effect during the bubble collapse stage is desired. Without this effect, the negative pullback of a JM after bubble collapse cannot be well explained.[21] Furthermore, the rich and interesting physics of microscopic bubble dynamics needs to be clarified, such as bubble growth behavior[26] and bubble collapse dynamics.[27-29] In particular, the presence of boundaries, such as an air-liquid interface, significantly influences the bubble collapse process;[30-33] however, their impact on JM propulsion has not been experimentally investigated.

In this work, we study the self-propulsion of hollow Pt-SiO_2 Janus micromotors moving just underneath an air-liquid interface. These hollow Janus micromotors (hJMs) are made of cenospheres, which are byproducts of coal powder combustion and have a hollow structure with a density of approximately 400 $kg\cdot m^{-3}$ and a diameter of about tens of microns. In the horizontal direction, owing to the subtle interactions between the microbubble and the hJM, an instantaneous speed of ~1 $m\cdot s^{-1}$ for the impulsive jetting flow is generated after bubble collapse. The energy stored by the bubble is focused by cavitation-induced jetting to propel the hJM, thus increasing the energy conversion efficiency by three orders of magnitude. In the perpendicular direction, the buoyancy of the bubble-hJM aggregate is counteracted by the vertical component of the jetting from the collapse of the microbubble. As a result, the hJM hovers up and down underneath the air-liquid interface. The complete mechanism is illustrated by flow visualization via particle tracking velocimetry (PTV) and computational fluid dynamic (CFD) simulations. The significant influence of the interface near the micromotor is verified by control experiments using solid Janus micromotors (sJMs) near a solid-liquid interface. The present bubble self-propulsion system is vividly described as an artificial 'microcatapult', analogous to the 'cavitation catapult' in nature;[34] the elastic launching of the payload is replaced by the dynamics of a single confined cavitation microbubble.

EXPERIMENTAL SECTION

Preparation of the hJMs. The cenospheres, which were made of silica, were purchased from Sino-steel Co. Ltd. The diameter of the cenospheres is approximately 20–50 μm. The Pt-SiO_2-type hJM was made by coating a layer of Pt onto one of the two hemispheres of a cenosphere. A droplet of the cenosphere solution was placed on a silicon wafer mounted on a spin coater. A rotating speed of 200 rpm was applied to spread the cenospheres uniformly on the wafer. After heat-drying, a monolayer of cenospheres was formed on the wafer. Then, an approximately 20-nm-thick Pt layer was evaporated using an Innotec E-beam evaporator. Due to the compact arrangement of the cenospheres, the Pt layer only covered the top half of the cenospheres, forming a double-faced Janus particle. Ultrasonic treatment was applied to keep the monodispersity of the hJMs prior to each experiment.

Self-propulsion of the hJMs. In the experiment, a droplet (70 μL) containing hJMs diluted in an H_2O_2 solution (2–5 vol %) was placed on a hydrophilic glass slide. The thickness of the sample solution was approximately 0.5–1 mm. The motions of the hJMs were observed with an inverted microscope (Nikon Eclipse Ti-U, with 20× or 40× objectives). A high-speed video camera (Phantom v7.3) was used to record the hJM motion and microbubble growth with frame rates of up to 85,000 fps. We obtained the positions of the hJMs and bubbles in each image by using the particle tracking method and further calculated their trajectories, bubble diameters, and bubble growth rate.[12] Polystyrene (PS) microspheres (diameter, 2 μm) were used as tracers to visualize the flow field of the strong, instantaneous jetting.

RESULTS AND DISCUSSION

Horizontal locomotion

Images of an hJM with a hemispherical coating of platinum and its inner hollow structure are shown in Figure 1a. In pure water, hJMs automatically float up toward the air-liquid interface owing to their lower apparent density. However, when hJMs are dispersed into a fuel solution, e.g., H_2O_2, their self-propelled movement occurs. The typical trajectory of an hJM (diameter $2R_{hJM} = 19.9$ μm; H_2O_2 concentration, 3%) according to the experimental video (video S1 in Supporting Information) is illustrated in Figure 1c. During a series of growth-collapse cycles of microbubbles, the hJM exhibits an approximately circular motion. The average speed of the hJM was calculated to be approximately 500 μm·s^{-1}, which corresponds to a speed-body length (S-BL) ratio of 25.

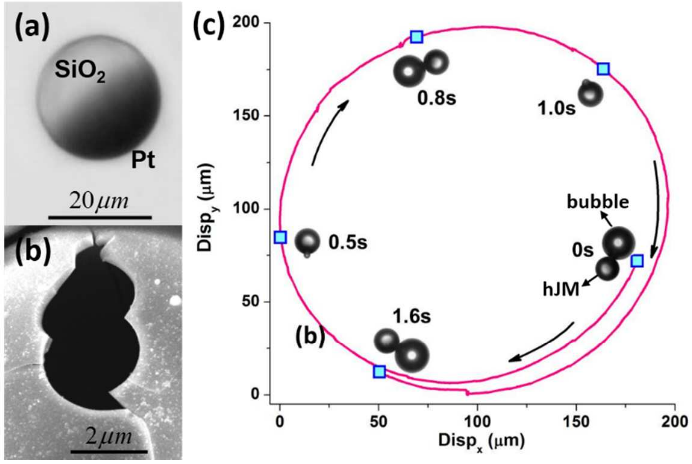

Figure 1. (a) A microscopy image of an hJM. (b) An SEM image of the broken shell of an hJM (in the experiments, only perfect hJMs were used). (c) The typical circular trajectory of a self-propelled hJM lasting 1.6 s.

The details of the hJM movement during a single cycle are shown in Figure 2a and 2b. The period from bubble formation to collapse lasts approximately 44 ms. According to the hJM displacement (L_p) vs. time (t) data (blue curve in Figure 2b), hJM motion is composed of three stages. In the first stage (0–8 ms), no bubble can be observed, and hJM displacement is approximately zero. This indicates that the period of restoration of the flow field is disrupted by a previous bubble. In the second stage (8–43.2 ms), a bubble appears and grows on the Pt hemisphere. This propels the hJM at an average speed of $V_p = 310 \pm 10$ μm·s^{-1}, which corresponds to an S–BL ratio of 15.5. The hJM locomotion in this stage is driven by diffusiophoretic forces and bubble growth, as mentioned in previous works[11, 21]. In the last stage (43.2–44 ms), the hJM exhibits a large instantaneous speed, following the microbubble collapse at approximately 43.2 ms. The maximum propulsion speed, V_p (red curves in Figure 2b), at this stage can reach up to ~10 cm·s^{-1}, which corresponds to a large S-BL ratio of 5000. Afterwards, the hJM decelerates in approximately 1 ms by the viscous drag force. These growth-collapse cycles can be repeated continuously to propel the hJM motion. The resultant Re numbers of the three stages in one cycle are ~0, ~10^{-2} and ~10, respectively, indicating a span of more than three orders of magnitude.

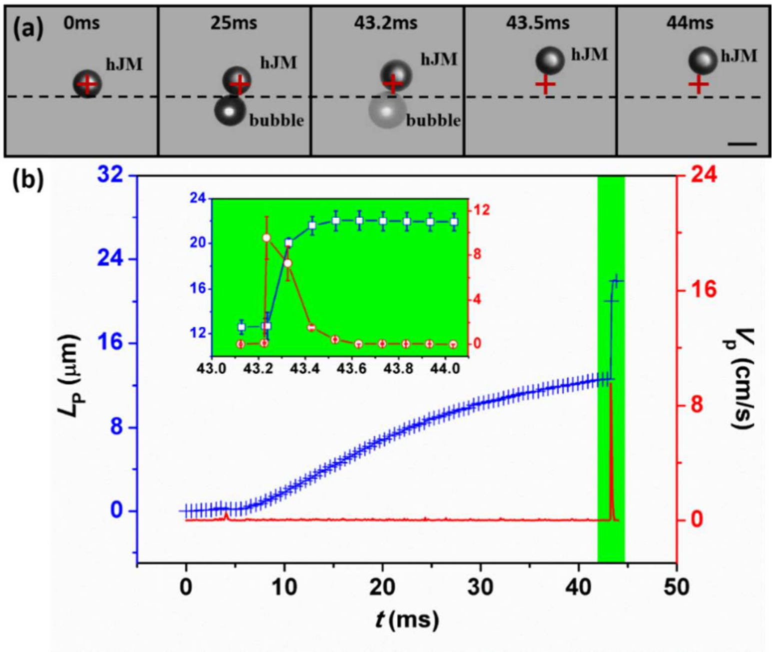

Figure 2. Experimental snapshots (a) and typical time-varied behavior in one single cycle (b). (a) The red cross denotes the initial position of a hJM. Scale bar, 20 μm. (b) The instantaneous displacement, L_p (blue curve with crosses), and speed, V_p (red curve), of hJM as a function of time, t, for a period of 44 ms. Inset: the data on hJM movement during bubble collapse (in the green region). The error bars for

displacement and speed are calculated based on standard deviations from n=8 cycles.

To clarify this confinement effect, a control experiment using sJMs located near a solid-liquid interface was performed and compared with the experimental results of the hJMs. Flow visualization experiments using polystyrene (PS) tracers for both hJMs and sJMs were carried out to capture the distinctive behavior of instantaneous flow during bubble collapse. Figure 3a illustrates the flow field around an hJM (created from a series of 30 consecutive images based on a video recorded at 9900 fps; see video S2 in Supporting Information). This clearly shows that a strong jetting flow was propelling the hJM forward immediately after the collapse of the bubble. A pair of vortices was observed in the wake region of the hJM, and the diameter of the jet core (the distance between the two vortices) was approximately 40 μm. This jet flow transfers the energy from the collapsing bubble into the propulsion of the hJM. The maximum speed of the core jet flow shown by the tracers was approximately 1 $\mathrm{m \cdot s^{-1}}$, i.e., 10 times larger than that of the hJM. Based on Kelvin's impulse theorem, which states that $Ft = \Delta(m_p V_p)$,[29] the maximum speed of the hJM can be estimated using the equation, $V_p = 3Ft/4\pi\rho_p R_p^3$. Since surface tension dominates bubble collapse, the equations of force and time should be $F \sim \pi R_b \sigma$ and $t \sim (\rho_{water} R_b^3/\sigma)^{0.5}$, respectively. Considering that the sizes of the bubbles and the hJM are on the same order of magnitude, the resultant value of $V_p \sim (\sigma\rho_{water}/\rho_p^2 R_p)^{0.5}$ is approximately 0.1–1 $\mathrm{m \cdot s^{-1}}$, which is consistent with our experimental result. Such speed will exert an effective impulse of $I \sim 10^{-13}$ N·s. To the best of our knowledge, this is the first study to directly identify microcavitation-induced jetting and its significant hydrodynamic effect on bubble propulsion, which unveils a new mechanism different from that of microbubble recoiling or microbubble-JM interactions proposed in recent works.[21, 23, 27, 28, 35]

Similar to the measured flow field of an hJM underneath the air-liquid interface shown in Figure 3a, Figure 3b shows the flow field around a sJM near the solid-liquid interface. Generally, the size of the bubbles generated in this case was much larger than that in the experiment using hJMs, and the bubbles were located on top of the sJM because of the buoyant force. The experimental videos showed that the sJM moved much slower (20–50 $\mu m \cdot s^{-1}$) during bubble formation and exhibited a clear backward displacement during bubble collapse (videos S3 and S4 in Supporting Information). At the horizontal focus plane across the bubble center, no liquid jetting was observed from the top view, and the flow direction pointed to the bubble center (white arrows in Figure 3b). At the plane between the sJM and the solid wall, the flow was found to be directed from the center to the outer region (red arrows in Figure 3b). The focus plane of the camera for Figure 3b was located near the bubble center, and so the tracers, indicated by the white arrows, were clearer and brighter than those shown by the red arrows. Based on the above information, we proposed a model, as shown in Figure 3c, to illustrate the vertical flow field around a sJM after bubble collapse. As a result, this flow field cannot propel the sJM significantly in the horizontal plane, and the efficiency of the propulsion is much lower due to the hindering effect of the wall.

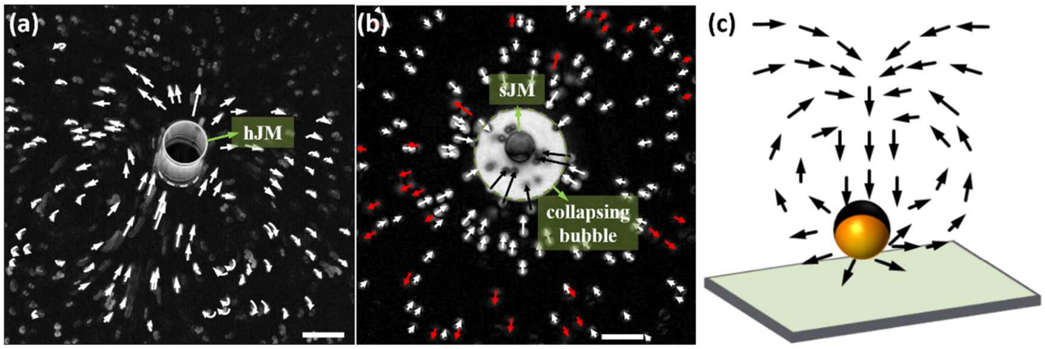

Figure 3. Images of the flow field during bubble collapse around (a) an hJM underneath the air-liquid interface and (b) a sJM near a solid wall. The white arrows represent the velocity vectors based on the motions of the tracers in the objective focus plane, and in (b) the red arrows represent the motions of the out-of-focus plane tracers. (c) A schematic diagram showing the vertical flow field around a sJM near a solid wall. Scale bar, 20 μm.

To better understand the locomotion of the microbubble, we further evaluated the propulsion performance based on the normalized microbubble size, $\gamma = R_b/R_p$ (Figure 4). There is a dependence of the propulsion styles quantified by the forward-to-backward index, β, on γ. $\beta = \log (L_{FW}/L_{BW})$ is defined as the logarithm of the ratio between the forward displacement (L_{FW}) by jetting and the backward displacement (L_{BW}) by the collapse of the bubble. Four different modes characterized by the hJM displacement styles were observed (see the four insets in Figure 4 and video S5 in Supporting Information). For small γ ($\gamma < 0.7$), the mode of 'moderate propulsion' was seen after a clear back-pull (symbol I), quantified by $0 < \beta << 1$. In this mode, energy from the collapsing bubble was too weak to propel the hJM forward significantly. For intermediate values of γ ($0.7 < \gamma < 1.5$), two possible modes could occur: one is ‘perfect propulsion’ with no backward displacement (symbol II, $\beta \rightarrow \infty$; also the case shown in Figure 2); the other is ‘strong propulsion’ with a small withdrawal (symbol III, $\beta = 0.5–1$). When $\gamma > 1.5$, it is surprising to observe that there is a sudden transition from the perfect propulsion mode ($\beta \rightarrow \infty$) to the opposite mode with a strong backward displacement (symbol IV, $\beta < 0$). In this case, the size of the bubble was so large that the confinement effect of the hJM was negligible, and the homogeneous shrinkage of the bubble predominated. As a result, the quasi-oscillatory motion proposed by Manjare et al. [2020] will cause the clear backward motion of the hJM. We emphasize that the competition between the hydrodynamic jet flow and the quasi-oscillatory motion after bubble collapse will determine the propulsion mode. Without the contribution of the hydrodynamic jet flow, the previous theories cannot well explain the instantaneous strong forward propulsion. Therefore, an intermediate microbubble size ($0.7 < \gamma < 1.5$) is crucial for generating a stronger forward propulsion by liquid jetting during collapse.

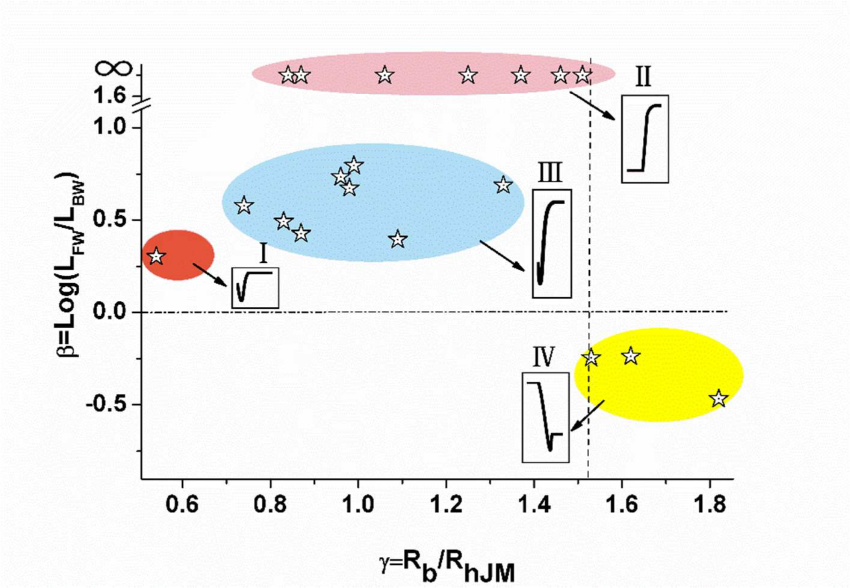

Figure 4. Different propulsion modes shown by the forward-to-backward index β versus the dimensionless microbubble size $\gamma = R_b/R_{hJM}$. The four insets show the typical displacement patterns occurring in the propulsion stage (corresponding to the pattern of displacement after microbubble collapse shown in the green region of Figure 2).

Vertical hovering

It would be interesting to examine whether the hJM continues swimming in the water or floating at the air-liquid interface. Some of the information on the vertical movement of the hJM can be obtained based on microscopic observations. We were able to locate the objective focus plane at the air-liquid interface by the highest position where the suspended PS tracers could still be clearly observed. Then, by adjusting the focus plane downwards, the hJM was estimated to be approximately 20–40 μm underneath the air-liquid interface. We could also exclude the possibility that the hJM was accidently trapped at the air-water interface and the significant contribution of the interfacial tension. If this situation occurred, the collapsing bubble would merge with air, inducing a vertical jet flow instead of a horizontal one, which was not observed in the experiment.

Another interesting question is how an hJM with a density smaller than water could overcome buoyancy and maintain its position underneath the air-liquid interface. The reason is attributed to the three-dimensional flow occurring in both the horizontal and vertical directions. In the vertical direction, because the constraint from the free surface (air-liquid interface) was weaker than that from the bulk liquid phase, the direction of the jet flow was towards the bulk liquid phase, which provides a mechanism to overcome the buoyancy. The strength of the vertical flow depends on the stand-off distance between the bubble and the air-liquid interface. The more closely the bubble approaches the interface, the stronger the jet flow is. Therefore, the hJM should periodically dive and float with the same small fluctuation in distance around a balance position due to the dynamic competition between the jet flow and the buoyancy. We refer to this adaptive vertical motion as 'dynamic hovering'.[36] Although it is difficult to experimentally obtain the real-time vertical position of the hJM due to the ultrafast collapse process, the fluctuation distance can be evaluated to be approximately 5.8 μm (see SI1 in Supporting Information) in terms of the balance between the buoyancy of the bubble-hJM aggregate and the Stokes drag force in the floating stage.

CFD simulations were performed to characterize the flow field during bubble collapse around a hJM (see SI2 and video S6 in Supporting Information). In the CFD bubble collapse simulation, the hJM was placed at the center of a cubic flow domain $[(40R_p)^3]$, and the gap between the interface (air-liquid or solid-liquid) and the hJM was $2R_p$. The finite volume method was used for numerical discretization, and the volume of fluid method was utilized for multiphase modeling (see SI2 in the Supporting Information). The time interval was set as 10^{-9} s in order to capture instantaneous information on the bubble collapse in the experiment. The simulation results from the top view (Figure 5a) are in good agreement with the experimental flow field shown in Figure 3a. For the side view, a jet flow pointing to the lower part of the hJM is clearly shown in Figure 5b. This flow, pushing the hJM downwards, resulted in the vertical dynamic hovering mentioned above, as illustrated in Figure 5d. In contrast, the simulation results in Figure 5c show that when the air-liquid interface is replaced by a solid-liquid interface, the jet flow pointed to the upper part of the hJM, which exhibits a totally different behavior due to the confinement effect. This result indicates that the flexible air-liquid interface makes a key contribution to the dynamic hovering of the hJM.

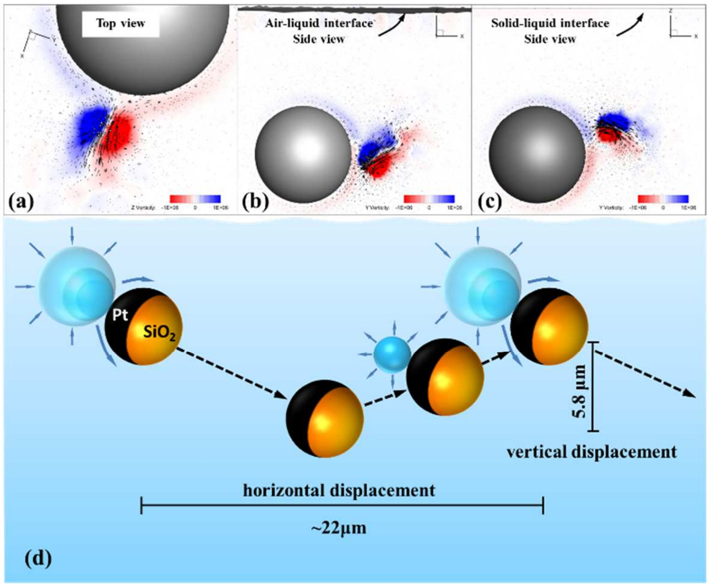
Top view
Air-liquid interface
Side view
Solid-liquid interface
Side view
(a)
Z Vorticity: -1E+06 0 1E+06
(b)
Y Vorticity: -1E+06 0 1E+06
(c)
Y Vorticity: -1E+06 0 1E+06
Pt
SiO2
5.8 µm
vertical displacement
horizontal displacement
~22µm
(d)

Figure 5. The CFD results of the flow field around a hollow hJM near an air-liquid interface from the (a) top view and (b) side view. (c) The distinct flow field near the liquid-solid interface. The arrow represents velocity, and the color represents vorticity. (d) A schematic drawing to show the dynamic hovering of an hJM near an air-liquid interface.

Previous theoretical studies have usually focused on how the curved profile of the air-liquid interface influences the balanced position of a spherical micromotor underneath the air-water interface.[37] The dynamic hovering described in the present work based on nonreciprocal vertical flow with a Re number ranging from ~0 to ~10 offers a novel mechanism. From our dynamic simulation, if the processes of both bubble growth and collapse are in the low Re regime, the net displacement of the hJM contributed by the cyclic bubbles must be zero. Then, buoyancy will always drive the hJM upwards. Breaking down the vertical flow reciprocity is the key to generating the dynamic hovering behavior that prevents lightweight underwater micromotors from floating.

Bubble Instability

Considering the importance of bubble size on propulsion efficiency (shown in Figure 4), we put forward a simplified model to explain the critical bubble size based on bubble instability. Assuming a quasi-steady state and a far-field reference pressure, p_{ref}, the internal pressure, p_b, of a bubble with radius R_b can be given by $p_{ref} + \sigma/R_b$, where σ is surface tension. With the presence of H_2O_2 in the solution, an O_2 bubble can be generated by the surface catalytic reaction, $2H_2O_2 \rightarrow 2H_2O + O_2$, and p_b is also the partial pressure of O_2. According to Henry's law, the required average mole concentration of dissolved O_2 around the bubble is $C_{O2,cri} = C_{H2O}(p_{ref}+\sigma/R_b)/\mathrm{H}$ (blue circles in Figure 6b), where $H = 4.4\times10^9$ Pa is the Henry coefficient for O_2 and $C_{H2O} = 5.6\times10^4$ mol·m^{-3} is the mole concentration of water.[26] Figure 6a shows the practical distribution of the concentration of dissolved oxygen, C_{O2}, for the typical experimental H_2O_2 concentration of 3% (vol/vol), based on the numerical model (see SI3 in Supporting Information). A sharp concentration gradient appears at the downstream side, as indicated by the purple squares along the downstream axis in Figure 6b. The converging of C_{O2} to $C_{\mathrm{O2,cri}}$ explains how mass transfer influences bubble growth. In the region of $C_{\mathrm{O2}} > C_{\mathrm{O2,cri}}$, the continuous growth of the bubble is supported by the sufficient background oxygen concentration. The larger concentration difference near the hJM leads to rapid growth. When the bubble size approaches the intersection point, the microbubble reaches its maximum radius. In the region of $C_{\mathrm{O2}} < C_{\mathrm{O2,cri}}$, the bubble ceases growing because of a limited supply of O_2. Once a small disturbance makes the bubble drift from this critical position, cavitation instability will be triggered, and the bubble begins to collapse. The experimental tendency of bubble growth is shown in Figure 6c. The maximum R_b observed in the experiment is approximately 13.5 μm. This is consistent with the prediction based on the intersection point, which indicates that the maximum bubble size is $2R_b \approx 25$ μm. In particular, two accurate exponential scaling laws of R_b during microbubble growth, $R_b \sim t^{1/2}$ and $R_b \sim t^{1/3}$, are observed. The dependency can be depicted by the Rayleigh-Plesset equation (see SI4 in Supporting Information) when either the surface tension or the ambient fluid pressure predominates. It is interesting to see that the Rayleigh-Plesset equation is still valid even considering the oxygen generation and dissolving. Also, ideally the derivation of the Rayleigh-Plesset equation requires the liquid around the microbubble should be infinite. However, even though the air-liquid interface is only about 20 – 50 μm above the bubble, we did not observe any noticeable influence from the air-liquid interface on the bubble dynamics. The gradually decreased growth rate indicated by the exponents of the above scaling laws is due to the decrease in the background oxygen concentration as the bubble grows. The complete bubble dynamics can be easily understood based on this theoretical framework.

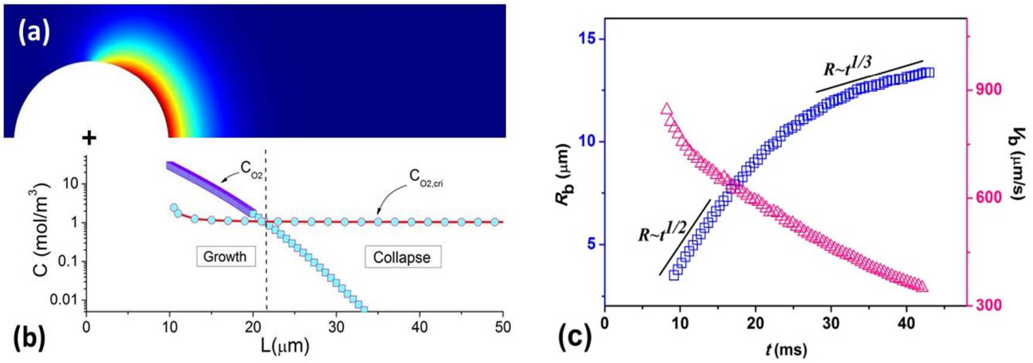

Figure 6. (a) The concentration field of dissolved O_2 around an hJM and (b) the distribution along the downstream axis. (c) The experimental data of bubble growth.

Analogy of a catapult

We demonstrate the observed instantaneous propulsion of the hJM as a microcavitation catapult by means of an analogy. In contrast to all other artificial catapults that use a crossbar to guide their movement direction, the present hJM, as the simplest microcatapult, has no such crossbar structure. However, a function similar to the crossbar is fully realized via dynamic interactions between the fluid and hJM through the bubble cavitation-collapse processes. Unlike the bubble collapse in an infinite flow field, when the bubble is confined in the vicinity of a boundary,[30-32] the rigid wall restricts the flow of the fluid to produce a jet flow towards the wall, while the flexible air-liquid interface promotes the flow to produce the jet flow away from the interface. We show that much of the sophistication here relies on the compact boundary combination between the air-liquid interface and the suspended hJM, where both boundaries guide the flow to a unique direction and the energy of the collapsing bubble is focused to propel the hJM rather than being dissipated and dispersed to the surrounding liquid.

The entire process of the cavitation catapult includes the power source of the catapult (surface catalytic reaction), energy storage (bubble growth), triggering mechanism (instability) and launching of the hJM (confinement-induced jetting flow). Qualitative nonreciprocal flow is responsible for the initiation of this process. However, a thorough understanding requires the full details of the lifetime of bubble dynamics and the bubble-hJM interaction. Further work will be devoted to the construction of an integral multi-timescale model.

It is interesting to compare the hJM catapult with natural and artificial counterparts. Sakes et al. have shown that the launching acceleration ranges from 6.6 *g* to approximately one million *g* based on the shooting mechanism in nature.[38] Our artificial hJM launches the catapult shooting within 10 μs, and thus, it could achieve an acceleration of approximately 1000 *g*. Thus, the impulsive force of cavitation jetting flow proved to be a powerful tool to realize complex motion control on the microscale.

Efficiency

We also estimated the energy transfer efficiency based on the energy variation of the system before and after bubble collapse. At the onset of bubble collapse, the bubble surface energy, defined by $E_b = 4\pi R_b^2\sigma \sim 10^{-9}$ J, reaches its maximum value, which is much larger than that of the translational kinetic energy ($\sim 10^{-18}$ J) of a recoiling bubble. Based on the observed speed, V_p, of the hJM after bubble collapse, the kinetic energy of the hJM is estimated to be $E_k = 2\pi\rho R_p^3 V_p^2/3 \sim 10^{-11}$ J. Therefore, the energy transfer efficiency, $\eta \sim E_k/E_b$, in the launching phase is approximately 1%. For the total energy transfer efficiency from the catalytic reaction phase to the micromotor motion phase, the present value is approximately 10^{-7}, and the previous value from similar experiments is 10^{-10}, which was estimated by Wang et al.[15] The present value shows an improvement of about three orders of magnitude for spherical Janus micromotors and is on the same order as that for the natural furious catapult mechanism.[38, 39]

Compared to the phoretic micro/nano-motor[11, 40], the present hJM has a dramatically higher propulsion speed and distinct dependency on the ‘fuel’ concentration. As analyzed by Ebbens et al.,[41] for a JM with a diameter of less than 10 μm, the propulsion speed is expected to be proportional to 1/R. The corresponding speed for a 10-μm JM is usually ~1 μm·s^{-1}, which is negligible. The present hJM configuration that generates the cavitation catapult has overcome this limitation by increasing the propulsion speed by over three orders of magnitude. Different from most of the micro/nano-motors that have a monotonic dependency of velocity on fuel concentration, herein, a suitable rather than plentiful fuel supply is the optimum swimming strategy. A higher concentration of H_2O_2 solution will produce more than one bubble around the hJM, and the excessive dissolved oxygen will prevent the bubbles from collapsing.

CONCLUSION

This study introduced the strong self-propulsion and dynamic hovering of hJMs by cyclical microbubble cavitation. The asymmetric collapse of a cavitation microbubble led to an instantaneous jet flow with a speed of up to 1 $m \cdot s^{-1}$ and a relatively high Re ~ 10. This hydrodynamic jetting is found to be a key propulsion effect after microbubble collapse, in contrast to microbubble recoiling or the JM-bubble interaction. Four different propulsion modes were identified based on the dimensionless size, γ. Boundary confinement and stand-off distance are two of the most important factors to generate effective propulsion. We further proposed that dynamic hovering is the locomotion mechanism to keep a lightweight micro-object swimming underneath an air-liquid interface, the buoyancy of which is counteracted by the vertical nonreciprocal flow. The combination of the relatively high Re and the focused energy of the jet flow improved the efficiency of the hJM up to 1%. The findings of this study shed light on the design of more efficient and adaptive micro-/nano-motors in autonomous micro-/nano-systems.

ASSOCIATED CONTENT

Supporting Information

The Supporting Information is available free of charge via the internet at http://pubs.acs.org.

SI: additional results from CFD simulation and analysis of the scaling law of bubble growth.

1. SI1: Evaluation of the vertical fluctuation distance of the hJM
2. SI2: CFD simulation of bubble collapse near different types of boundaries
3. SI3: CFD simulation of the O_2 concentration around the hJM

4. SI4: Scaling law of bubble growth by using the Rayleigh-Plesset equation

Video:

1. Video S1: Circular motion and perfect propulsion
2. Video S2: Flow visualization of the jetting flow near the hJM
3. Video S3: Flow visualization at the upper plane of the sJM near the solid-liquid interface
4. Video S4: Flow visualization at the bottom plane of the sJM near the solid-liquid interface
5. Video S5: Four propulsion styles with different γ
6. Video S6: Computational fluid dynamics (CFD) simulation of bubble collapse near two types of boundaries

AUTHOR INFORMATION

Corresponding Author

*E-mail: cuihaihang@xauat.edu.cn

*E-mail: zhengxu@lnm.imech.ac.cn

ORCID

Xu ZHENG: 0000-0002-2398-9283

Author Contributions

Leilei Wang and Li Chen contributed equally to this work. Leilei Wang prepared the micromotor and conducted the motion testing. Li Chen simulated the processes of bubble collapse. Hai-hang Cui, Xu Zheng and Zhan-hua Silber-Li designed the experiment. Jing Zhang finished the flow visualization by PIV experiment. Jin-ming Duan and Lei Wang conducted the theoretical analysis for the dynamic hovering of the micromotor. All authors made contributions to the writing of the paper.

Notes

The authors declare no competing financial interest.

ACKNOWLEDGMENT

The authors thank Dr. Wei Wang from HIT for his fruitful discussion. The authors are grateful for the financial support from the National Natural Science Foundation of China (Grants No. 11572335, 11272322 and 11602187), the Major Science and Technology Program for Water Pollution Control and Treatment (Grant No. 2014ZX07305-002-01), the CAS Key Research Program of Frontier Sciences (QYZDB-SSW-JSC036), and the CAS Strategic Priority Research Program (XDB22040403).

REFERENCES

(1) Wang, J.; Gao, W., Nano/Microscale Motors: Biomedical Opportunities and Challenges. *ACS Nano* **2012,** 6, 5745-5751.

(2) Li, J.; Singh, V. V.; Sattayasamitsathit, S.; Orozco, J.; Kaufmann, K.; Dong, R.; Gao, W.; Juradosanchez, B.; Fedorak, Y.; Wang, J., Water-driven micromotors for rapid photocatalytic degradation of biological and chemical warfare agents. *ACS Nano* **2014,** 8, 11118-11125.

(3) Gao, W.; Wang, J., Synthetic micro/nanomotors in drug delivery. *Nanoscale* **2014,** 6, 10486-10494.

(4) Abdelmohsen, L. K. E. A.; Peng, F.; Tu, Y.; Wilson, D. A., Micro- and nano-motors for biomedical applications. *J. Mater. Chem.* **2014,** 2, 2395-2408.

(5) Ma, X.; Wang, X.; Hahn, K.; Sánchez, S., Motion Control of Urea-Powered Biocompatible Hollow Microcapsules. *ACS Nano* **2016,** 10, 3597-3605.

(6) Rojas, D.; Juradosánchez, B.; Escarpa, A., “Shoot and Sense” Janus Micromotors-Based Strategy for the Simultaneous Degradation and Detection of Persistent Organic Pollutants in Food and Biological Samples. *Anal. Chem.* **2016,** 88, 4153-4160.

(7) Gao, W.; Wang, J., The environmental impact of micro/nanomachines: a review. *ACS Nano* **2014,** 8, 3170-3180.

(8) Eskandarloo, H.; Kierulf, A.; Abbaspourrad, A., Nano- and micromotors for cleaning polluted waters: focused review on pollutant removal mechanisms. *Nanoscale* **2017,** 9, 13850-13863.

(9) Paxton, W. F.; Kistler, K. C.; Olmeda, C. C.; Sen, A.; St Angelo, S. K.; Cao, Y.; Mallouk, T. E.; Lammert, P. E.; Crespi, V. H., Catalytic nanomotors: autonomous movement of striped nanorods. *J. Am. Chem. Soc.* **2004,** 126, 13424-13431.

(10) Fournier-Bidoz, S.; Arsenault, A. C.; Manners, I.; Ozin, G. A., Synthetic self-propelled nanorotors. *Chem. Commun.* **2005,** 4, 441-443.

(11) Howse, J. R.; Jones, R. A. L.; Ryan, A. J.; Gough, T.; Vafabakhsh, R.; Golestanian, R., Self-motile colloidal particles: from directed propulsion to random walk. *Phys. Rev. Lett.* **2007,** 99, 048102-4.

(12) Zheng, X.; ten Hagen, B.; Kaiser, A.; Wu, M.; Cui, H.; Silberli, Z.; Löwen, H., Non-Gaussian statistics for the motion of self-propelled Janus particles: experiment versus theory. *Phys. Rev. E* **2013,** 88, 032304-11.

(13)Anderson, J. L., Colloid Transport by Interfacial Forces. *Annu. Rev. Fluid. Mech.* **1989,** 21, 61-99.

(14)Ebbens, S.; Tu, M. H.; Howse, J. R.; Golestanian, R., Size dependence of the propulsion velocity for catalytic Janus-sphere swimmers. *Phys. Rev. E* **2012,** 85, 020401-4.

(15)Wang, W.; Chiang, T. Y.; Velegol, D.; Mallouk, T. E., Understanding the Efficiency of Autonomous Nano- and Microscale Motors. *J. Am. Chem. Soc.* **2013,** 135, 10557-65.

(16)Mei, Y.; Huang, G.; Solovev, A. A.; Ureña, E. B.; Mönch, I.; Ding, F.; Reindl, T.; Fu, R. K. Y.; Chu, P. K.; Schmidt, O. G., Inside Front Cover: Versatile Approach for Integrative and Functionalized Tubes by Strain Engineering of Nanomembranes on Polymers *Adv. Mater.* **2008,** 20, 4085-4090.

(17)Solovev, A. A.; Mei, Y.; Bermúdez, U. E.; Huang, G.; Schmidt, O. G., Catalytic microtubular jet engines self-propelled by accumulated gas bubbles. *Small* **2009,** 5, 1688-1692.

(18)Sanchez, S.; Ananth, A. N.; Fomin, V. M.; Viehrig, M.; Schmidt, O. G., Superfast Motion of Catalytic Microjet Engines at Physiological Temperature. *J. Am. Chem. Soc.* **2011,** 133, 14860-14863.

(19)Purcell, E. M., Life at low Reynolds number. *Am. J. Phys.* **1977,** 45, 3-11.

(20)Ren, Y.; Liu, X.; Liu, W.; Tao, Y.; Jia, Y.; Hou, L.; Li, W.; Jiang, H., Flexible particle flow-focusing in microchannel driven by droplet-directed induced-charge electroosmosis. *Electrophoresis.* **2017,** 39, 597-607.

(21)Manjare, M.; Yang, B.; Zhao, Y. P., Bubble driven quasioscillatory translational motion of catalytic micromotors. *Phys. Rev. Lett.* **2012,** 109, 128305-5.

(22)Manjare, M.; Yang, B.; Zhao, Y. P., Bubble-Propelled Microjets: Model and Experiment. *J. Phys. Chem. C* **2013,** 117, 4657-4665.

(23)Wang, S.; Wu, N., Selecting the Swimming Mechanisms of Colloidal Particles: Bubble Propulsion versus Self-Diffusiophoresis. *Langmuir.* **2014,** 30, 3477-86.

(24)Pinchasik, B. E.; Skirtach, A. G., Mimicking bubble use in nature: propulsion of Janus particles due to hydrophobic-hydrophilic interactions. *Small* **2014,** 10, 2670-7.

(25)Orozco, J.; Juradosánchez, B.; Wagner, G.; Gao, W.; Vazquezduhalt, R.; Sattayasamitsathit, S.; Galarnyk, M.; Cortés, A.; Saintillan, D.; Wang, J., Bubble-propelled micromotors for enhanced transport of passive tracers. *Langmuir.* **2014,** 30, 5082-7.

(26)Yang, F.; Manjare, M.; Zhao, Y.; Qiao, R., On the peculiar bubble formation, growth, and collapse behaviors in catalytic micro-motor systems. *Microfluid Nanofluid* **2017,** 21, 6-6.

(27)Borkent, B. M.; Arora, M.; Ohl, C. D.; De Jong, N.; Versluis, M.; Lohse, D.; Morch, K. A.; Klaseboer, E.; Khoo, B. C., The acceleration of solid particles subjected to cavitation nucleation. *J. Fluid. Mech.* **2008,** 610, 157-182.

(28)Poulain, S.; Guenoun, G.; Gart, S.; Crowe, W.; Jung, S., Particle Motion Induced by Bubble Cavitation. *Phys. Rev. Lett.* **2015,** 114, 214501-5.

(29)Blake, J. R.; Leppinen, D. M.; Wang, Q., Cavitation and bubble dynamics: the Kelvin impulse and its applications. *Interface Focus* **2015,** 5, 20150017-20150017.

(30)Blake, J. R.; Taib, B. M.; Doherty, G., Transient cavities near boundaries. Part 1. Rigid boundary. *J. Fluid. Mech.* **1986,** 170, 642-650.

(31)Blake, J. R.; Taib, B. B.; Doherty, G., Transient cavities near boundaries. Part II: Free surface. *J. Fluid. Mech.* **1987,** 181, 197-212.

(32)Gregorčič, P.; Petkovšek, R.; Možina, J., Investigation of a cavitation bubble between a rigid boundary and a free surface. *J. Appl. Phys.* **2007,** 102, 27-28.

(33)Liu, W.; Ren, Y.; Tao, Y.; Chen, X.; Yao, B.; Hui, M.; Bai, L., Control of two-phase flow in microfluidics using out-of-phase electroconvective streaming. *Phys. Fluids.* **2017,** 29, 112002-13.

(34)Noblin, X.; Rojas, N. O.; Westbrook, J.; Llorens, C.; Argentina, M.; Dumais, J., The fern sporangium: a unique catapult. *Science* **2012,** 335, 1322-1322.

(35)Zwaan, E.; Gac, S. L.; Tsuji, K.; Ohl, C. D., Controlled Cavitation in Microfluidic Systems. *Phys. Rev. Lett.* **2007,** 98, 401-414.

(36)Ristroph, L.; Childress, S., Stable hovering of a jellyfish-like flying machine. *J. R. Soc. Interface* **2014,** 11, 20130992-20130992.

(37)Crowdy, D.; Lee, S.; Samon, O.; Lauga, E.; Hosoi, A. E., A two-dimensional model of low-Reynolds number swimming beneath a free surface. *J. Fluid. Mech.* **2010,** 681, 24-47.

(38)Aimée, S.; Marleen, V. D. W.; Henselmans, P. W. J.; Van, L. J. L.; Dimitra, D.; Paul, B., Shooting Mechanisms in Nature: A Systematic Review. *PLoS. ONE* **2016,** 11, 1-46.

(39)Forterre, Y., Slow, fast and furious: Understanding the physics of plant movements. *J. Exp. Bot.* **2013,** 64, 4745-4760.

(40)Moran, J. L.; Posner, J. D., Phoretic Self-Propulsion. *Annu. Rev. Fluid. Mech.* **2017,** 49, 511-540.

(41)Ebbens, S.; Tu, M. H.; Howse, J. R.; Golestanian, R., Size dependence of the propulsion velocity for catalytic Janus-sphere swimmers. *Phys. Rev. E* **2012,** 85, 605-624.

Table of Contents Graphic

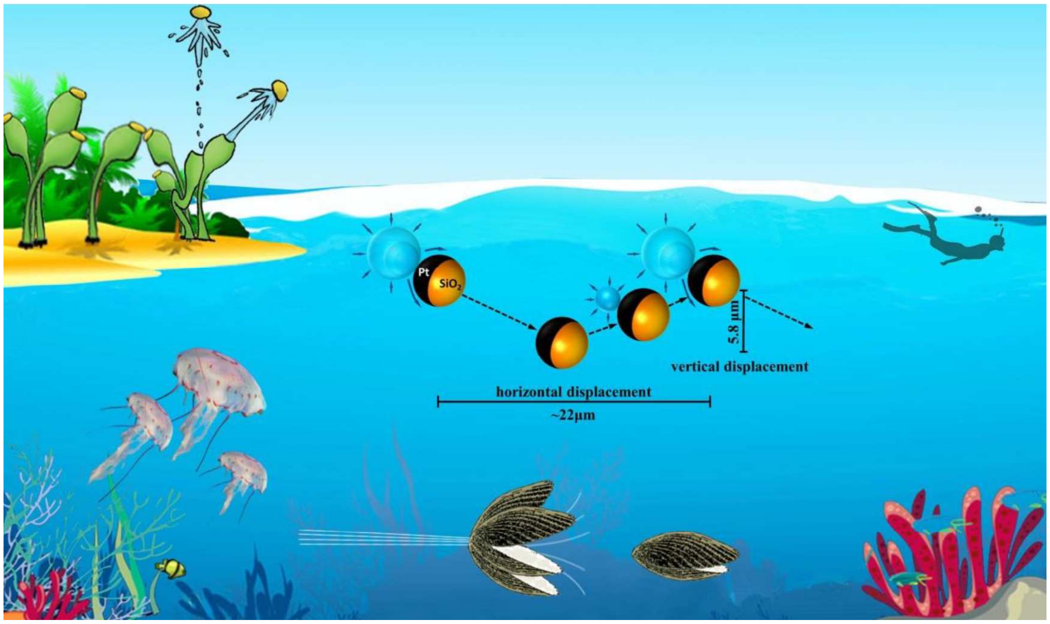

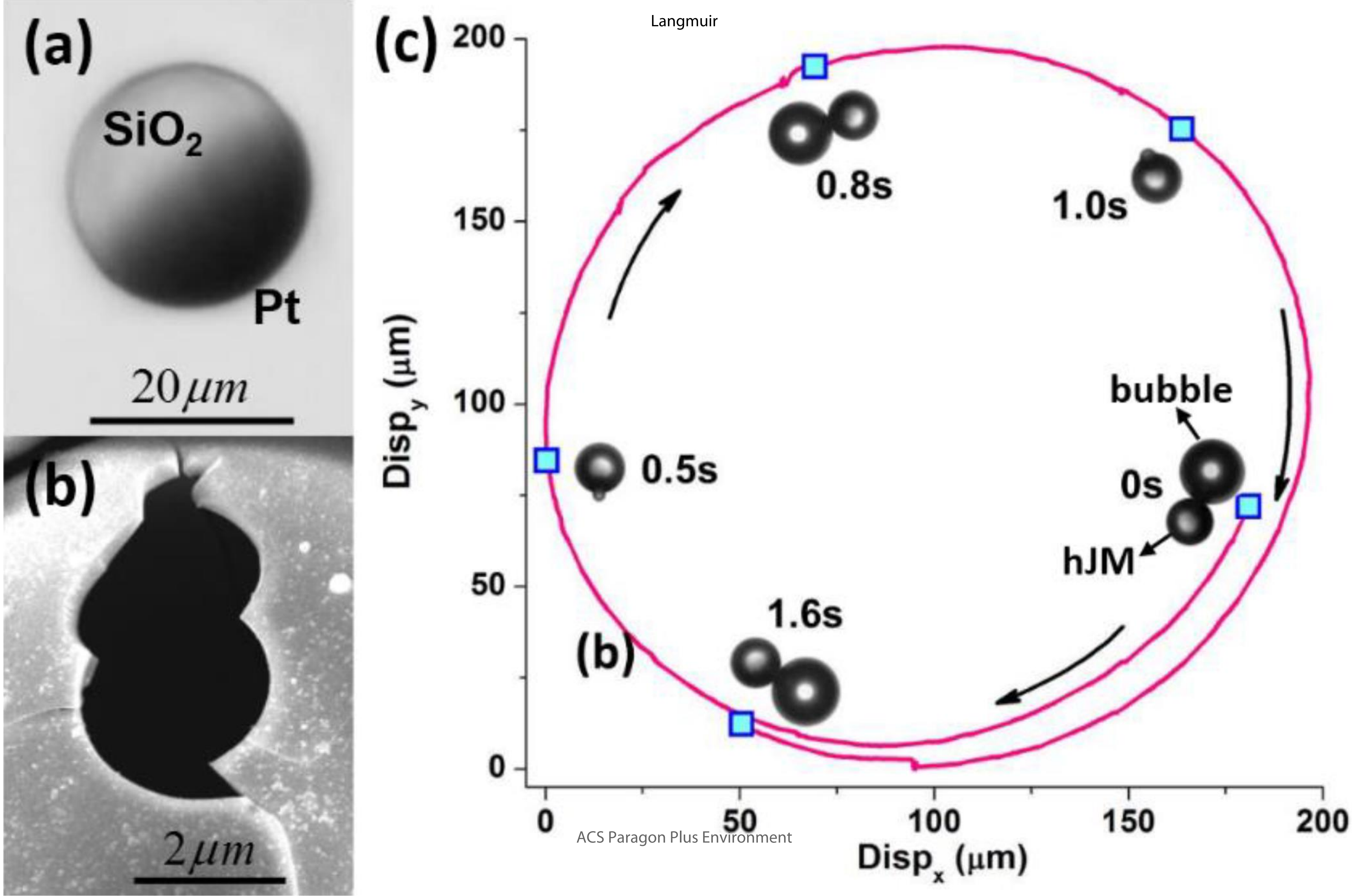
(a)
SiO$_2$
Pt
20 μm
(b)
2 μm
(c)
Disp$_y$ (μm)
Disp$_x$ (μm)
0
50
100
150
200
0
50
100
150
200
0.8s
1.0s
0.5s
bubble
0s
hJM
1.6s
(b)

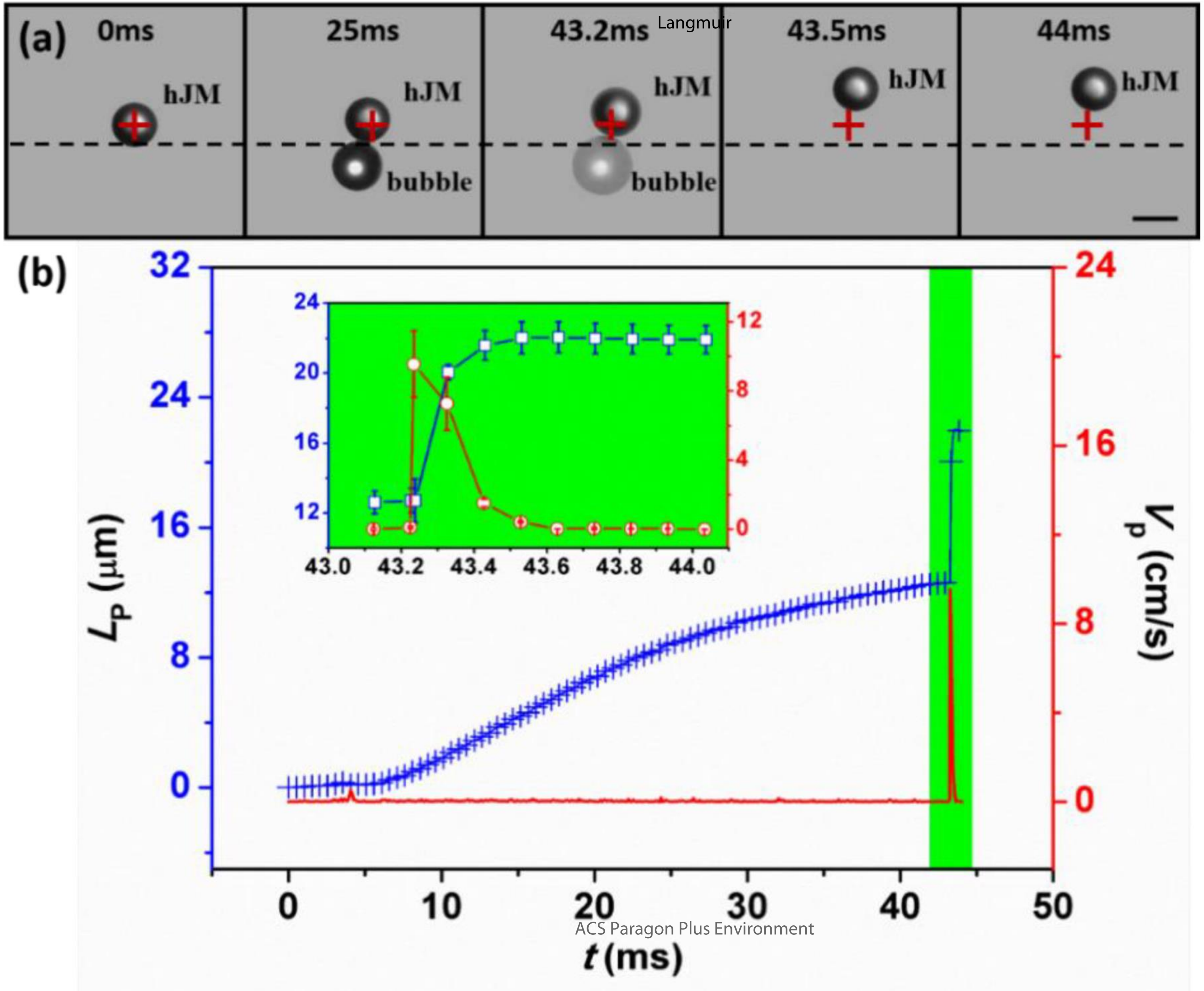
(a)
0ms
25ms
43.2ms
43.5ms
44ms
hJM
bubble
(b)
L_P (μm)
32
24
16
8
0
V_p (cm/s)
24
16
8
0
t (ms)
0
10
20
30
40
50
24
20
16
12
12
8
4
0
43.0
43.2
43.4
43.6
43.8
44.0

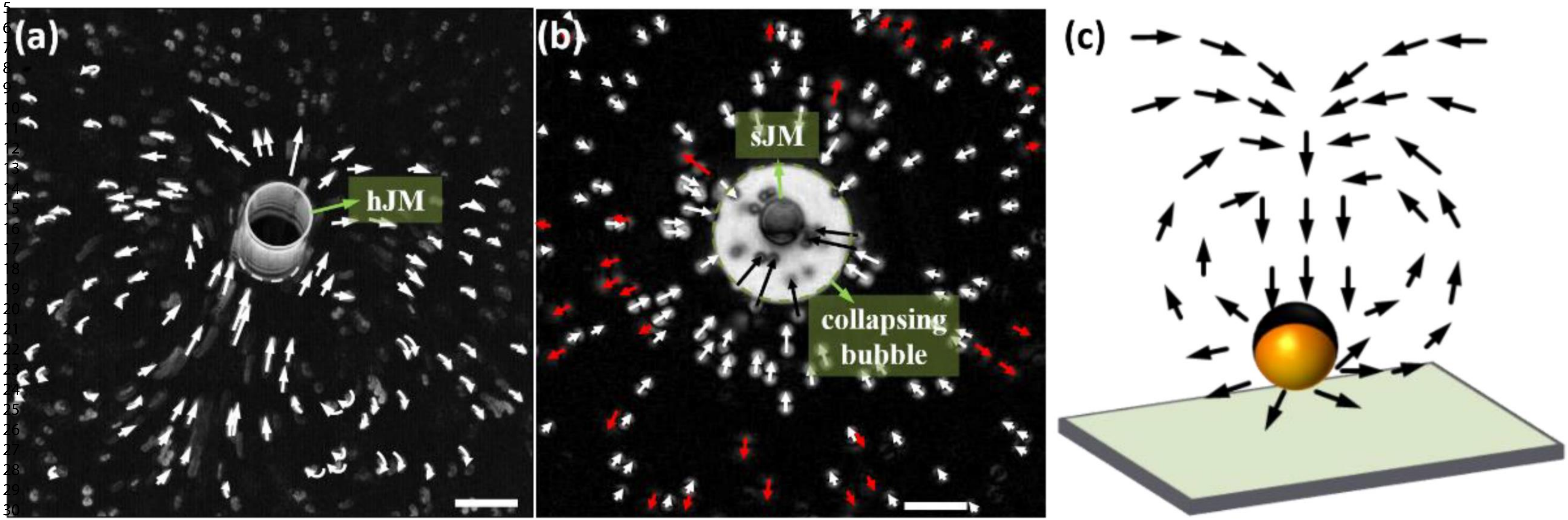
(a)
hJM
(b)
sJM
collapsing bubble
(c)

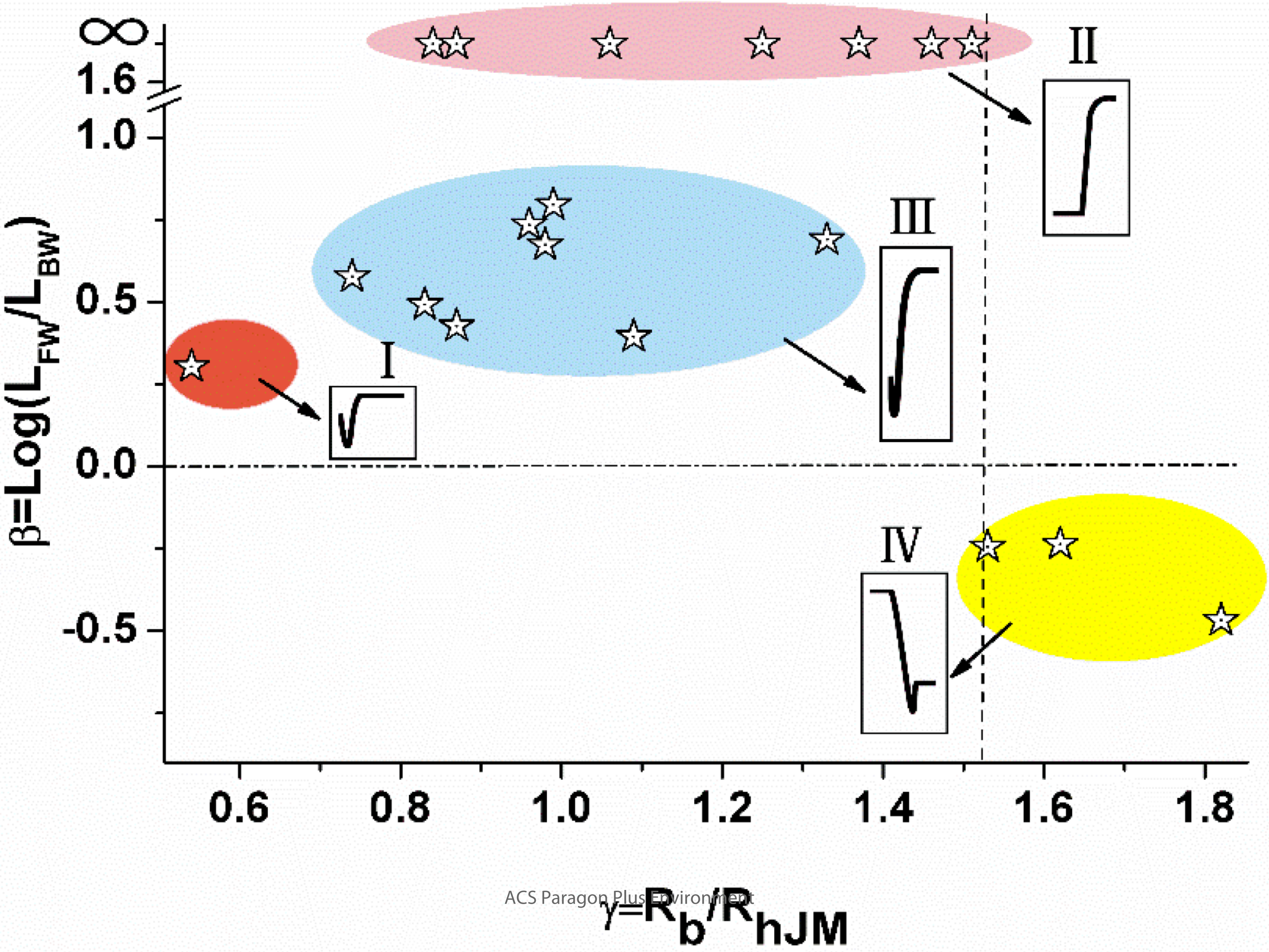
∞
1.6
1.0
0.5
0.0
-0.5
β=Log(L_FW/L_BW)
0.6
0.8
1.0
1.2
1.4
1.6
1.8
γ=R_b/R_hJM
I
II
III
IV

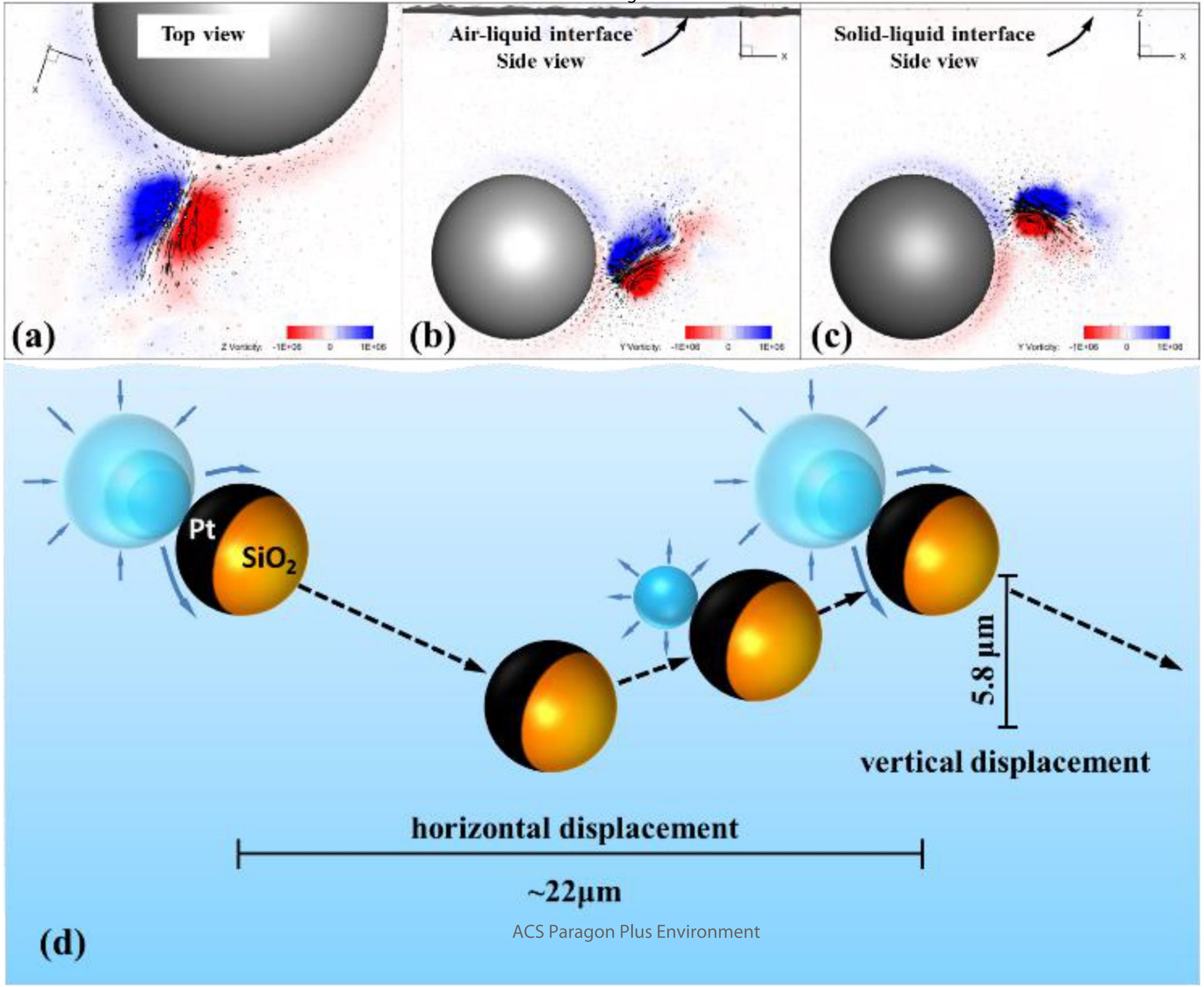
Top view
Air-liquid interface
Side view
Solid-liquid interface
Side view
x
y
z
(a)
Z Vorticity: -1E+06 0 1E+06
(b)
Y Vorticity: -1E+06 0 1E+06
(c)
Y Vorticity: -1E+06 0 1E+06
Pt
SiO$_2$
5.8 μm
vertical displacement
horizontal displacement
~22μm
(d)

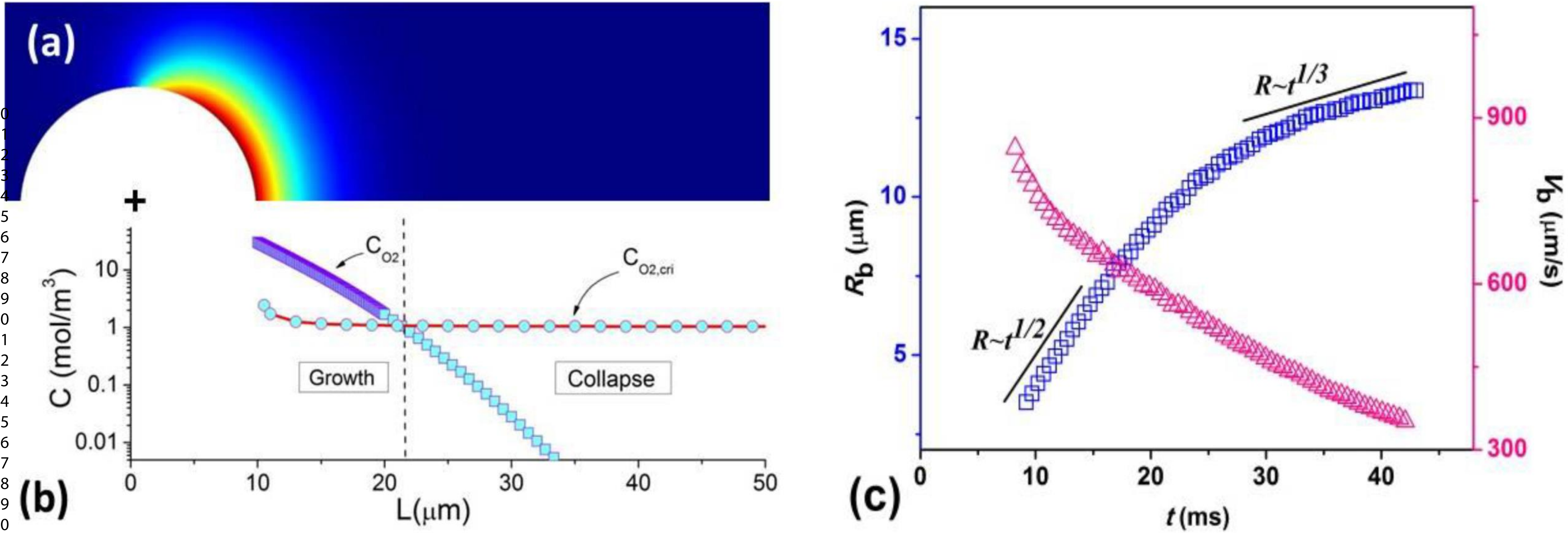
(a)
+
C_{O2}
$C_{O2,cri}$
C (mol/m^3)
10
1
0.1
0.01
Growth
Collapse
0
10
20
30
40
50
L(μm)
(b)
R_b (μm)
15
10
5
$R \sim t^{1/3}$
$R \sim t^{1/2}$
v_b (μm/s)
900
600
300
0
10
20
30
40
t (ms)
(c)